NANO · MICRO small
www.small-journal.com

In Situ N-Doped Graphene and Mo Nanoribbon Formation from $Mo_2Ti_2C_3$ MXene Monolayers

*Rafael Gregorio Mendes, Huy Quang Ta, Xiaoqin Yang, Wei Li, Alicja Bachmatiuk, Jin-Ho Choi, Thomas Gemming, Babak Anasori, Liu Lijun, Lei Fu, Zhongfan Liu, and Mark Hermann Rümmeli**

Since the advent of monolayered 2D transition metal carbide and nitrides (MXenes) in 2011, the number of different monolayer systems and the study thereof have been on the rise. $Mo_2Ti_2C_3$ is one of the least studied MXenes and new insights to this material are of value to the field. Here, the stability of $Mo_2Ti_2C_3$ under electron irradiation is investigated. A transmission electron microscope (TEM) is used to study the structural and elemental changes in situ. It is found that $Mo_2Ti_2C_3$ is reasonably stable for the first 2 min of irradiation. However, structural changes occur thereafter, which trigger increasingly rapid and significant rearrangement. This results in the formation of pores and two new nanomaterials, namely, N-doped graphene membranes and Mo nanoribbons. The study provides insight into the stability of $Mo_2Ti_2C_3$ monolayers against electron irradiation, which will allow for reliable future study of the material using TEM. Furthermore, these findings will facilitate further research in the rapidly growing field of electron beam driven chemistry and engineering of nanomaterials.

Since the isolation of an atomic layer of graphene was demonstrated in 2004, the family of 2D materials has been steadily growing.[1] These new 2D materials include borophene,[2] phosphorene,[3,4] boron nitride,[5] transition metal dichalcogenides,[6] oxides,[7] and hydroxides.[8] 2D layered materials can be isolated as monolayers. This often imparts unique properties that have been of interest in a wide range of applications, including nanoelectronics,[9] energy storage,[10,11] and biomedical applications.[12] Transition metal carbides and nitrides, also known as MXenes, are a new class of 2D materials that were first introduced in 2011 and which have attracted significant research focus. The first MXene, Ti_3C_2, was synthesized by exfoliating layered Ti_3AlC_2 with

Dr. R. G. Mendes, Dr. H. Q. Ta, X. Yang, W. Li, Dr. A. Bachmatiuk, Prof. J.-H. Choi, Prof. M. H. Rümmeli
Soochow Institute for Energy and Materials Innovations
College of Physics
Optoelectronics and Energy
Collaborative Innovation Center of Suzhou Nano Science and Technology
Soochow University
Suzhou 215006, China
E-mail: mhr1@suda.edu.cn

Dr. R. G. Mendes, Dr. H. Q. Ta, X. Yang, W. Li, Dr. A. Bachmatiuk, Dr. J.-H. Choi, Prof. M. H. Rümmeli
Key Laboratory of Advanced Carbon Materials and Wearable Energy Technologies of Jiangsu Province
Soochow University
Suzhou 215006, China

Dr. R. G. Mendes, Dr. H. Q. Ta, Dr. A. Bachmatiuk, Dr. T. Gemming, Prof. M. H. Rümmeli
Leibniz Institute for Solid State and Materials Research Dresden
P.O. Box 270116, Dresden D-01171, Germany

X. Yang, Prof. L. Lijun
School of Energy and Power Engineering
Xi'an Jiaotong University
No. 28, Xianning West Road, Xi'an, Shaanxi 710049, China

The ORCID identification number(s) for the author(s) of this article can be found under https://doi.org/10.1002/smll.201907115.

DOI: 10.1002/smll.201907115

Dr. A. Bachmatiuk
Polish Center for Technology Development (PORT)
Ul. Stabłowicka 147, Wrocław 54-066, Poland

Dr. A. Bachmatiuk, Prof. M. H. Rümmeli
Centre of Polymer and Carbon Materials
Polish Academy of Sciences
M. Curie-Skłodowskiej 34, Zabrze 41-819, Poland

Prof. B. Anasori
Department of Materials Science & Engineering, and A. J. Drexel Nanomaterials Institute
Drexel University
Philadelphia, PA 19104, USA

Prof. B. Anasori
Department of Mechanical and Energy Engineering and Integrated Nanosystems Development Institute
Purdue School of Engineering and Technology
Indiana University-Purdue University Indianapolis
Indianapolis, IN 46202, USA

Prof. L. Fu
College of Chemistry and Molecular Science
Wuhan University
Wuhan 430072, China

Prof. Z. Liu
Center for Nanochemistry
Beijing Science and Engineering Centre for Nanocarbons
Beijing National Laboratory for Molecular Sciences
College of Chemistry and Molecular Engineering
Peking University
Beijing 100871, China

Prof. M. H. Rümmeli
Institute of Environmental Technology
VSB-Technical University of Ostrava
17. Listopadu 15, Ostrava 708 33, Czech Republic

hydrofluoric acid.[13] Ti_3AlC_2 is a member of a larger family of layered carbides and nitrides referred to as MAX phases.[14] MXenes have a chemical formula of $M_{n+1}X_nT_x$, where M is an early transition metal, and X is carbon and/or nitrogen, and $n = 1$, 2 or 3. T_x refers to MXenes surface terminations such as =O, −F, and −OH.[15–17] In this study, we used $M_{n+1}X_n$ notation when referring to MXenes and do not show T_x for brevity.

The number of MXenes is rapidly increasing and many more have been theoretically predicted. In 2015, density functional theory (DFT) was used to predict the existence of two new subfamilies of MXenes ($M'_2M''C_2$ and $M'_2M''_2C_3$) and successfully synthesized TiC_2 layers sandwiched by molybdenum layers (Mo-layers) using the precursor MAX phases, Mo_2TiAlC_2 and Mo_2TiAlC_2.[18] The exfoliation of the MAX phases is initially selectively etched and then exfoliated using an intercalant, which finally yielded individual MXene layers of Mo_2TiC_2 and $Mo_2Ti_2C_3$, respectively. These individual layers are then dispersible in aqueous solution. Little research has been conducted on these structures, but they show promise for electrochemical energy storage and electromagnetic interference shielding.[18,19] Notably, very little is known regarding the behavior of individual layers of MXenes when exposed to electron beam irradiation and the published works focused on the use of external heating or a combination of heating and electron irradiation.[20–23]

The nanoengineering and the design of materials with bespoke properties is competitive and has fueled the need for a better understanding of the fundamental properties of MXenes. Several recent studies have explored the interactions between imaging electron beams and other 2D materials for their synthesis and engineering, including with graphene,[24,25] boron nitride[26,27] and transition metal dichalcogenides (TMDs).[28] The most relevant damage processes on 2D materials are knock-on damage and radiolysis. Knock-on damage refers to an elastic interaction between the incident electron and the specimen. A material has a knock-on threshold energy which is dependent on the material, the bond strength, crystal lattice and atomic weight of the atoms. Electrons with energy above the knock-on threshold energy can cause atomic displacements in the specimen. Radiolysis refers to an inelastic interaction between the incident electron beam and the specimen. This can lead to sample degradation, including loss of crystallinity and mass loss.[20,29] Within electron microscopy there is a trend of exploiting these electron beam-specimen interactions in a useful manner.[21,30] Such investigations are important for developing strategies for nanomaterial synthesis and engineering at the atomic scale.

Electron microscopy in situ investigations on Ti_3C_2 flakes have been conducted and the formation of new thicker layers of MXenes, such as Ti_4C_3 and Ti_5C_4 was observed.[22] Their work focused on using in situ heating (500 °C) and electron irradiation to promote changes in the Ti_3C_2 lattice. In another study, the surface of $Ti_3C_2T_x$ layers by in situ heating from room temperature up to temperatures of 750 °C was characterized and the behavior of F and O atoms that are inherently present on the MXene surface was monitored.[20] Their investigations suggested that at temperatures above 550 °C, fluorine atoms start to desorb from the surface and the subsequent vacancies are then occupied by O atoms. This heating process may serve as a means to tailor specific functionalization of the MXene. Further investigations again used elevated temperatures to study the surface chemistry, thermal stability, and the change in electrical properties of a few MXenes. Their results indicated that residual molecules present on the surface of the MXenes can decompose into different species.[31,32] For example, the delamination process of MXenes using tetrametylammonium hydroxide (TMAOH) can add N-containing species on the surface of the MXene flakes. [31]

The delamination process of MXenes can also introduce point defects. Such defects are important because they can regulate the physiochemical properties of MXenes. For example, the characterization of the atomic structure of intrinsic point defects on monolayered Ti_3C_2 and showed that the etchant (hydrofluoric acid) can introduce different types of point defects and the concentration of these defects can be tuned by adjusting the concentration of the etchant.[33] The atomic structure degradation of Nb_2C MXene flakes left in vacuum for up to 5 days as well as after exposure to air were investigated.[23] Their work demonstrated that Nb adatoms facilitated the attraction of O, creating oxidation clusters that degrade the entire MXene structure.

Although a few studies have investigated the atomic structure of MXenes in terms of their intrinsic defects and functionalization cause by the delamination process and/or in situ heating, no specific studies have explicitly investigated the interactions of electron beams with MXenes at the atomic level. Fundamental questions regarding the influence of lattice intrinsic defects and the effect of electron irradiation on this class of 2D materials remain unanswered. Few techniques are capable of probing materials at the atomic scale. Cs aberration corrected scanning/transmission electron microcopy (STEM) is a potential technique for the study of MXenes that could provide unique insight into the structural stability of the MXene lattice under electron irradiation. Irradiation with electrons from the imaging beam causes elastic and inelastic interactions that lead to various types of electron-beam-induced damage and changes to the specimen.

This study aimed to explore $Mo_2Ti_2C_3$ monolayers under an imaging electron beam using a transmission electron microscope operating at 300 kV and 80 kV. An intact area of the $Mo_2Ti_2C_3$ monolayer was exposed to various electron beam doses. The dynamics of the structural changes were evaluated using high resolution transmission electron microscopy and STEM imaging and electron energy loss spectroscopy (EELS) to yield elemental information.

TEM investigations revealed that the $Mo_2Ti_2C_3$ flakes were irregular in shape and varied in size (**Figure 1**A). The diffraction pattern shown in the inset presents a hexagonal arrangement, as expected. High-resolution TEM image of the pristine MXene (nonirradiated) is presented in Figure 1B. The dynamic transformations from electron irradiated $Mo_2Ti_2C_3$ monolayers were examined in detail. Figure 1C shows a schematic of a pristine $Mo_2Ti_2C_3$ monolayer under electron beam irradiation. Irradiation of the $Mo_2Ti_2C_3$ flake leads to a number of electron-induced structural changes. Two primary changes were observed, namely the formation of low contrast membranes and ribbons (Figure 1D), and the formation of high-contrast ribbon-like structures (Figure 1E). However, no clear difference in contrast was observed, which is in agreement with the in-plane ordering of $Mo_2Ti_2C_3$.[34] Contrast differences

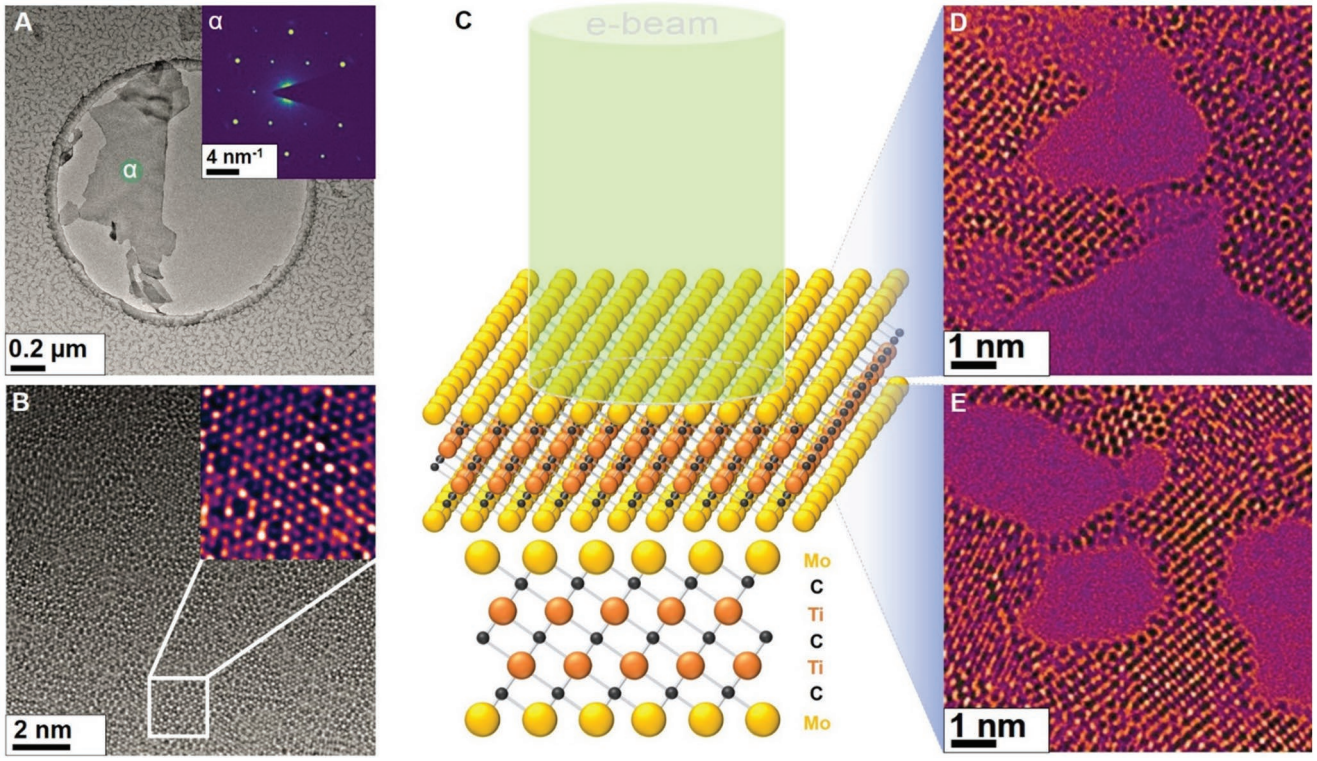

Figure 1. A) $Mo_2Ti_2C_3$ flake sizes are typically a few micrometers laterally. The region labeled as α depicts where the SAED was collected, which is shown in the inset. B) High-resolution TEM image of the $Mo_2Ti_2C_3$ flake. A magnified area of the lattice is shown in the inset. C) A stick and ball illustration of the $Mo_2Ti_2C_3$ monolayer (3D structure at the top and side view at the bottom) during electron beam irradiation, and high-magnification TEM images (with false color) showing the resultant new structures after extended electron irradiation, namely, D) N-doped graphene membranes and E) Mo nanoribbons.

can be more easily observed in the cross-section image of the $Mo_2Ti_2AlC_3$ MAX phase, which was demonstrated in an earlier study when $Mo_2Ti_2C_3$ was first introduced.[18]

Once the presence of $Mo_2Ti_2C_3$ flakes were confirmed across the grid, a few $Mo_2Ti_2C_3$ flakes were selected for further investigation. The selected areas for electron exposure were as intact as possible, and were free from visible holes, defects or grain boundaries. This ensured that any observed structural changes were due to the electron beam. The areas were exposed to different electron doses ranging between 2×10^4 and 3×10^4 e Å^{-1} for time periods up to 385 s. The selected areas of $Mo_2Ti_2C_3$ were irradiated using an electron beam at an acceleration voltage of 300 kV for six min.

A typical result is presented as a collection of snapshots (Figure S1, Supporting Information), which illustrates the numerous electron-beam driven structural changes that occur. The irradiated area of the lattice was of ≈30 × 30 nm^2. The $Mo_2Ti_2C_3$ lattice was observed to undergo many different changes before completely rupturing. In the early stages of irradiation exposure (≈2 min), the $Mo_2Ti_2C_3$ lattice remains stable across the majority of the sample area (Figure S1A, Supporting Information). This is an indication that the $Mo_2Ti_2C_3$ monolayers are sufficiently stable to conduct imaging tests. With extended irradiation, electron beam driven changes were observed and were characterized by the appearance of regions with a lighter contrast, as indicated by the red arrow in Figure S1B (Supporting Information). This is indicative of the removal of heavier elements (Ti and Mo) and/or the rearrangement of atoms. With further irradiation, an increasing number of the light contrast membranes were observed and holes began to appear. The low contrast membranes and holes are indicated by red and yellow arrows, respectively, in Figure S1C (Supporting Information). Similar effects were observed when using electron accelerations of 80 kV, although the rate of change was lower. These observations suggested that sputtering (knock-on damage) was the dominant process by which atoms were removed, and it has been established that radiolysis usually increases with decreasing acceleration voltage.[29] The time frame for these changes are typically 0 s to ≈385 s at 300 kV and 0 s to ≈570 s at 80 kV. Further study of this aspect would be required to provide greater detail. As exposure to electron irradiation continued, the holes began to rapidly expand and fuse with other holes. This resulted in the formation of a network of nanoribbons, as indicated by the white arrows (Figure S1E–G, Supporting Information). The nanoribbons appeared as either light or dark contrast. The formation of nanoribbon networks usually occurred within 60 s. Elemental analysis of heavily irradiated areas suggested the presence of both C and Mo rich regions. A detailed demonstration of the dynamic processes involved was provided in Movies S1–S4 (Supporting Information).

The regions of low contrast represent the N-doped graphene membranes and are discussed in more detail later. These areas were distributed randomly across the irradiated area. Once

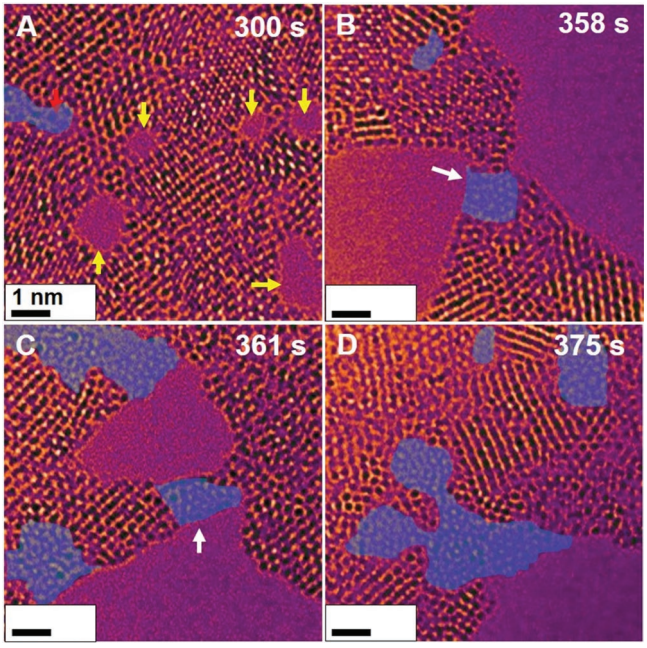

Figure 2. High-magnification microscopy images (with false color) of the formation of N-doped graphene membranes and pores after extended electron irradiation of a $Mo_2Ti_2C_3$ monolayer (total exposure: 6 min with a 300 kV acceleration voltage) at time A) 300 s, B) 358 s, C) 361 s, and D) 375 s. Yellow arrows indicate pores and white arrows N-doped graphene ribbons. Blue shading indicates N-doped graphene membranes or ribbons.

formed, changes to these regions occurred relatively quickly (≈4–6 s) even when the electron dose was reduced to about 6×10^3 e Å^{-1}. This suggests that the ribbon structures are quite sensitive to electron irradiation viz., have limited stability. The thinning process is shown in **Figure 2**, which captures the process from 300 to 375 s. After 300 s only very small (<1 nm) low contrast regions could be observed (false blue shading). However, the lateral size and number of membranes increased with extended irradadion. Careful examination of the membranes indicates that the lattice structure includes pentagonal, hexagonal and heptagonal structures, characteristic of disordered or doped sp^2 carbon suggesting the layers can be graphene-like. In addition, holes appeared and grew until all material was lost and only a vacuum remained. Additional detail for this process is provided in Movie S3 and Figure S2 (Supporting Information). The low contrast membranes seem to comprise a single or bi-layer (Figure S2, Supporting Information). The fact that materials is lost after about 6 min indicates that the atoms, Mo and Ti, are removed from the structure and suggests the structure is unstable, which is in contrast to the Ti_3C_2 MXene behavior, where homoepitaxial growth of hexagonal TiC layers were observed under electron beam irradiation and heating.[22]

To confirm the graphene-like structure and removal of Mo and Ti atoms, we used EELS in STEM mode to provide local elemental information. To minimize damage, fast scan rates were used. **Figure 3** shows EELS data obtained for different irradiation stages. Figure 3A shows the intact materials and the corresponding EELS spectrum (Figure 3B). The EELS spectrum indicated the presence of Mo (227 eV), C (284 eV), and Ti (460 eV), as expected for $Mo_2Ti_2C_3$. N (401 eV) was also detected. The presence of N is indicative of TBA^+ (tetrabutylammonium) remaining on the surface of MXene as a result of the delamination process, which is in agreement with a previous study on Mo_2TiC_2 that was synthesized following a similar process.[32] Lattice changes were observed after ≈300 s of irradiation, such as reducing amounts of high-contrast material and

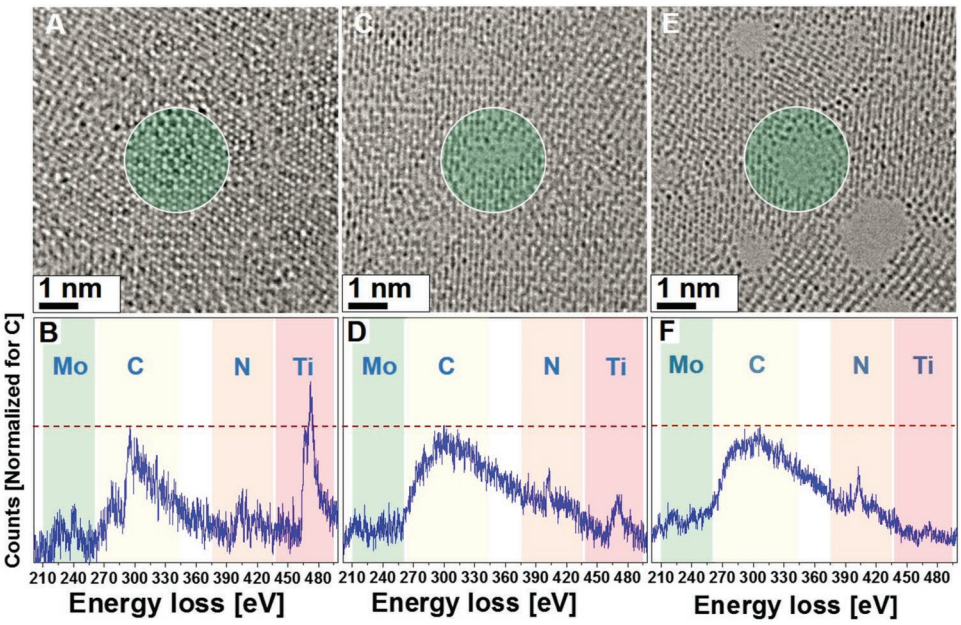

Figure 3. Microscopy images and EELS spectra showing the changes in structure and elemental composition during the formation of an N-doped graphene membrane. A,C,E) Microscopy images of the $Mo_2Ti_2C_3$ structural changes during extended electron irradiation that led to the formation of an N-doped graphene membrane. B,D,F) EELS spectra for each microscopy image showing the elemental changes that occurred during the structural changes. The green-shaded circles indicate the approximate area where EELS signals were collected.

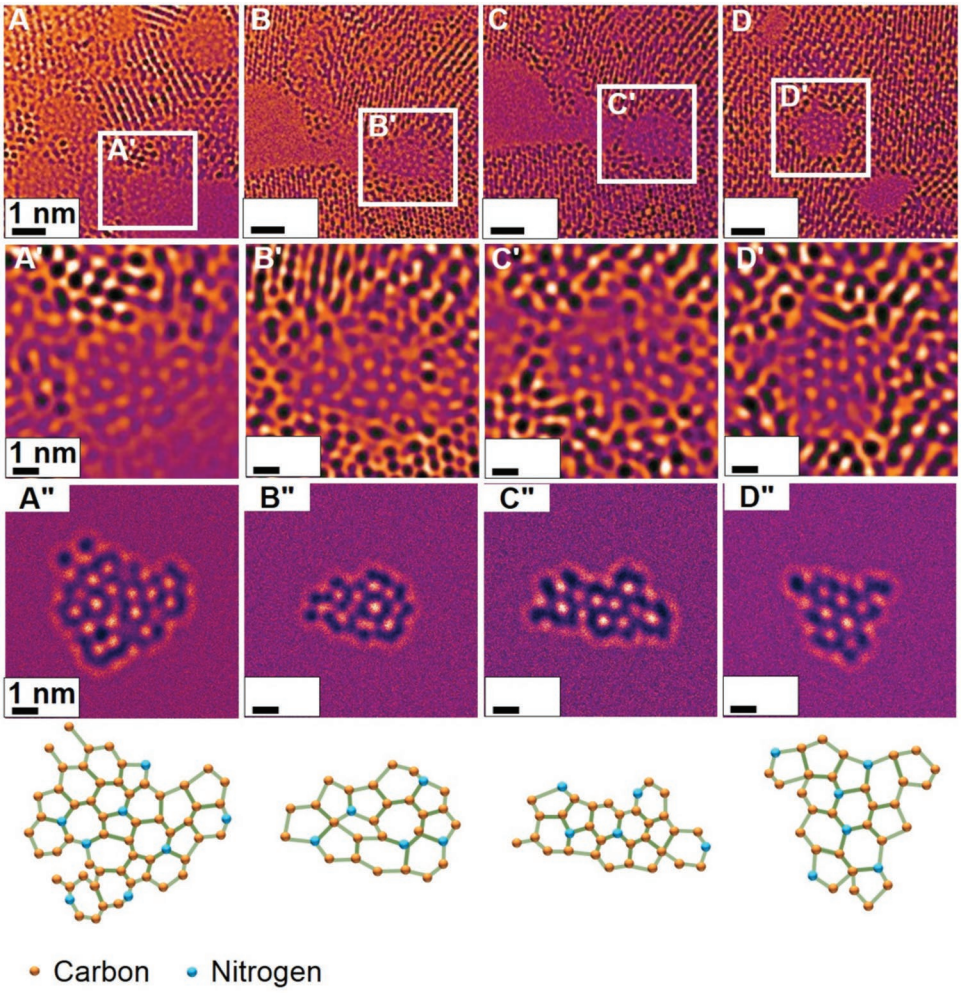

Figure 4. Dynamic structure change of N-doped graphene membranes under electron irradiation. A–D) Microscopy images of an N-doped graphene membrane exhibiting structural changes upon electron irradiation. A'–D') Magnified FFT-filtered images of the regions containing the N-doped graphene membrane, exhibiting a defective structure composed of pentagons, hexagons, and heptagons, are observable (7×7 nm^2). A"–D") Image simulations based on the stick and ball model, which confirm the presence of an N-doped graphene membrane undergoing structural changes while under electron irradiation.

the appearance of the low contrast graphene-like membrane (Figure 3C). The EELS spectrum in Figure 3D indicates that levels of Mo and Ti were largely reduced, and that the C and N peaks remained, although the C peak had broadened. The broader C edge indicated changes in its bonding configuration. With further irradiation of ≈60 s, the relative intensities of the Mo and Ti edges were significantly reduced with almost no discernable Ti peak, suggesting that Ti was preferentially removed over Mo. The edges for C and N remained strong and were indicative that the low contrast membranes and ribbons consisted of N-doped graphene (Figure 3E,F).

The low contrast membranes degraded rapidly under the electron beam and this was associated with defective (doped) graphene.[35–37] Mo and Ti were preferentially removed from the $Mo_2Ti_2C_3$ monolayers during irradiation, which left C and N species to rearrange and form small N-doped graphene membranes or ribbons. The presence of nitrogen is attributed to the introduction of N-containing molecules used during delamination in the $Mo_2Ti_2C_3$ monolayer production process. Previous studies have shown that MXene delamination with tetrabutylammonium hydroxide (TBAOH) or TMAOH, leaves TBA^+ or TMA^+ molecules on the surface.[31,32] Both studies demonstrated that these molecules decompose into $NH_2/NH_3/NH_4^+$ species under heating. The current study suggests a similar phenomenon driven by electron beam irradiation instead of heating. The electron irradiation of TBA^+ molecules led to the formation of NH_x species which may have decomposed to provide a source of N. The N species interacted with C to form N-doped graphene. High-magnification images, stick and ball models of the N-doped graphene membranes and their corresponding image simulations are provided in **Figure 4**. The image simulations match well with the obtained microscopy images supporting N-doped graphene sections form.

The production of nanoribbons and nanowires from 2D materials via electron beam irradiation has been demonstrated for TMDs.[38,39] This study is the first demonstration of nanoribbon formation from a MXene. **Figure 5** shows the various steps for Mo nanoribbon formation. Figure 5A shows the

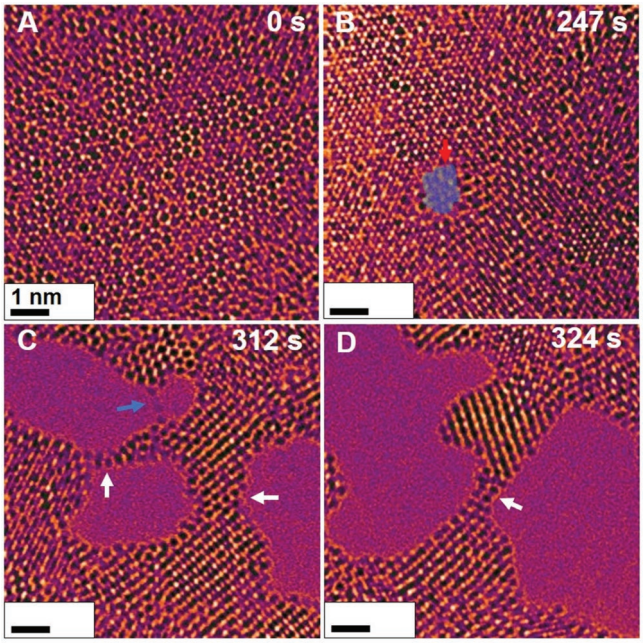

Figure 5. High-magnification microscopy images showing the formation of a Mo nanoribbon through extended electron irradiation of a $Mo_2Ti_2C_3$ monolayer and subsequent Mo nanoribbon formation at A) 0 s, B) 247 s, C) 312 s, and D) 324 s. White arrows indicate Mo nanoribbons. Red arrow indicates an N-doped graphene membrane.

intact material. Early N-doped graphene membranes begin to form under continued irradiation (Figure 5B). With further irradiation, holes continued to form and, in some cases, merged to form a Mo nanoribbon (Figure 5C,D). The stability of the ribbons deteriorated with increassing irradiation dose. Different electron doses may slow down the process, but no clear differences in the phenomena are observed with different doses.

Figure 6 shows the structural changes to a nanoribbon under electron irradiation (Figure 6A–E), after which the ribbon collapsed completely. The in situ data indicated significant changes in the lattice structure. As discussed earlier, the EELS data suggested preferential ejection of the Ti species over Mo. Thus, the high-contrast nanoribbons are likely composed of Mo, and this was confirmed by local EELS measurements (Figure 6G). Figure 6A shows a Mo ribbon with the central area matching a (110) orientation[40] (yellow arrow). The regions above and below have different orientations.

At some junctions, the change was not clear (red arrow), suggesting an amorphous-like region. The multiple crystalline orientations were dynamic under the electron irradiation. The entire bottom section of the ribbon later changed to a single crystal orientation and was bound to the top part of the ribbon with a different orientation (Figure 6B). The multiple crystal orientations switching to a single orientation can be observed in Figure 6C. Continued irradiation of the single crystal ribbon resulted in material loss until an Mo atomic chain formed and collapsed (Figure 6D,E). Movie S4 and Figure S3 (Supporting Information) shows these dynamic processes in greater detail.

The central and thinner area connecting the two sides of the Mo nanoribbon was very unstable and changed multiple times before eventual breakage. **Figure 7**A depicts a moment when the nanoribbon is changing structure and appears in an almost amorphous state. Figure 7B shows the nanoribbon with various crystal orientations. Figure 7C presents the same image with false coloring to highlight the different orientations. Figure 7D–F provides the d spacing's for the different highlighted areas. Metallic Mo can be presented with different crystalline configurations that vary according to its stability and prevalence.[41] Figure 7D presents a hexagonal-like structure, whereas Figure 7E,F presents more cubic-like. It is important to mention that the measured lattice spacings can vary strongly due to strain making accurate indexation challenging.

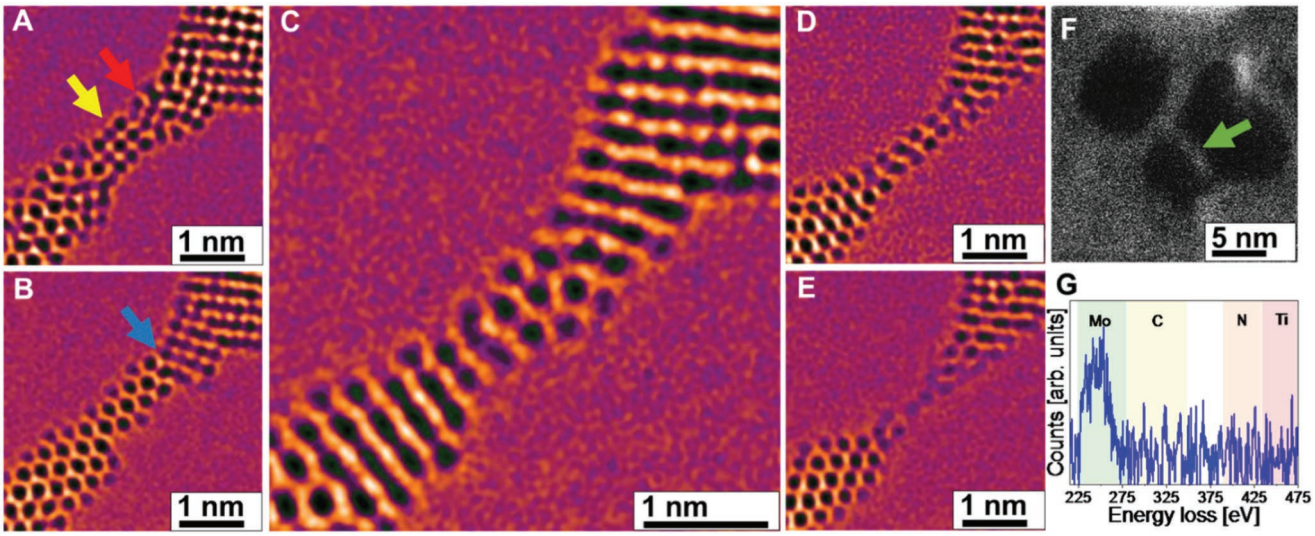

Figure 6. Structural changes to a Mo nanoribbon and final collapse upon electron beam irradiation. A–E) FFT-filtered snapshots of the ribbon over time, where the yellow arrow indicates the Mo (110) orientation of the nanoribbon that was bound to an amorphous-like area, indicated by the red arrow. F) Fast acquisition HAADF image of a Mo nanoribbon and G) EELS of the nanoribbon in (F) confirming it comprises Mo.

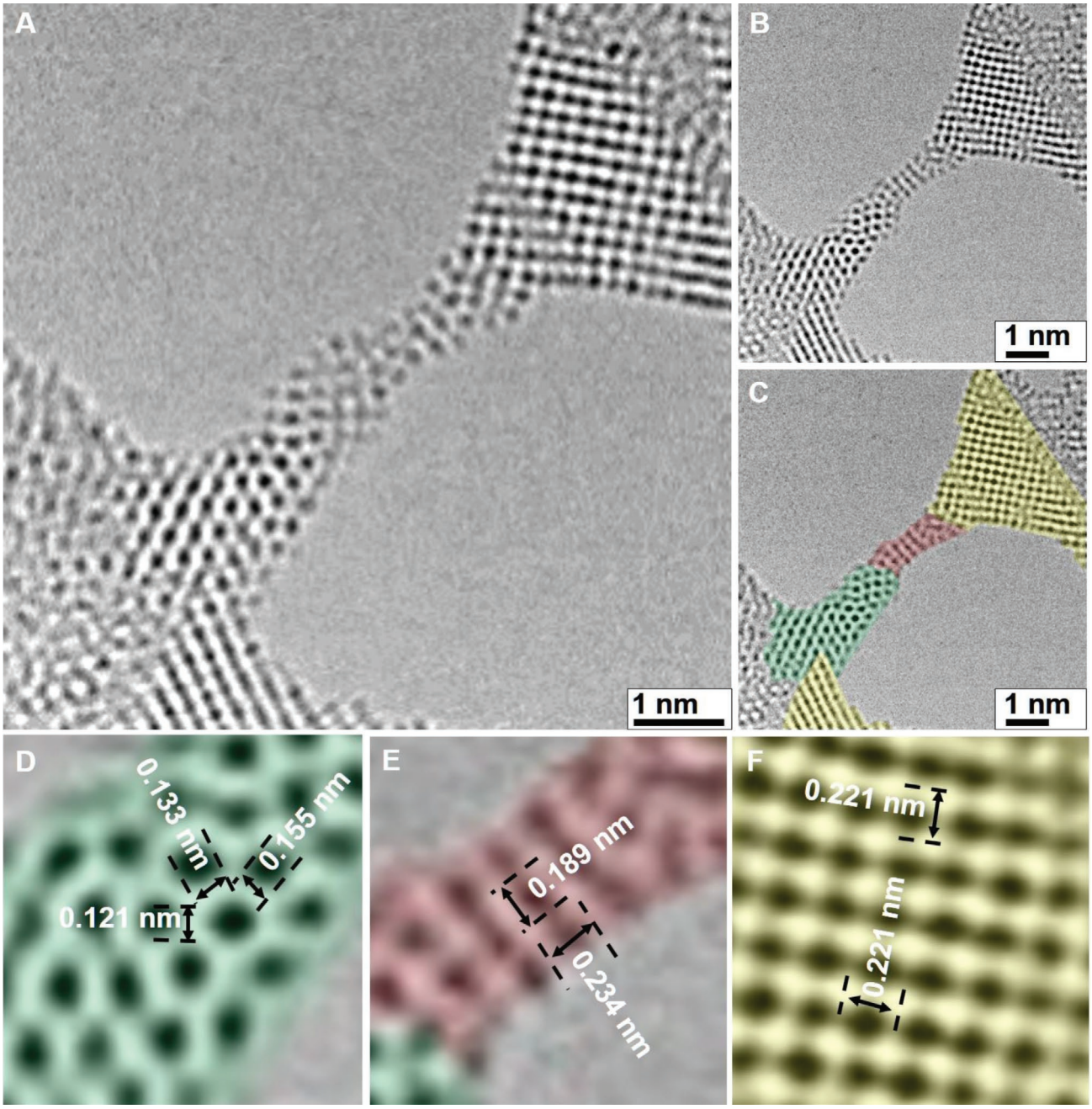

Figure 7. Dynamic changes of Mo nanoribbon under electron irradiation. A) A snapshot a Mo nanoribbon. The central and thinner area connecting the two sides is unstable and changes a number of times before eventual breakage. B,C) The different grain orientations involved. D–F) *d* spacings for the different sections of the Mo nanoribbon.

In general, we observed dissimilar behavior and stability for the $Mo_2Ti_2C_3$ MXene under e-beam irradiation as compared to a report on Ti_3C_2 under both electron irradiation beam and in situ heating.[22] While in both studies displacement and re-arrangement of atoms due to the electron beam were observed, unlike Ti_3C_2 where hexagonal TiC layers were formed,[22] we observed the destruction of the $Mo_2Ti_2C_3$ monolayers, as well as the formation of new nanomaterials, namely, N-doped graphene and Mo crystals that sputter to form Mo nanoribbons. Although the majority of the study utilized a 300 kV acceleration voltage, we observed the same processes at 80 kV, albeit at a slower rate, indicating that the destruction of $Mo_2Ti_2C_3$ in which Ti is removed preferentially over Mo and C, is probably due to the lower sputtering threshold of Ti. The remaining Mo and C species then rearranged independently to ultimately yield Mo nanoribbons and N-doped graphene rather than a molybdenum carbide phase (e.g., MoC, MoC_2 or Mo_4C_3). The other possible reason for the lower stability of this MXene compared with Ti_3C_2 could be related to the selective etching and delamination process. The use of a Ti_3C_2 MXene that was

processed and delaminated in a milder etchant (hydrochloric acid and lithium fluoride) and delaminated without TBAOH differs from exfoliation methods with a harsher etching conditions, which can lead to a higher number of transition metal vacancies.[33] Additionally, the use of TBAOH leads to a smaller flake size, possibly due to more defects occurring during the delamination process. The higher number of defects could contribute to a reduced stability of $Mo_2Ti_2C_3$. In addition the bonding configurations are obviously different when compared to other MXenes.

We also conducted formation energy calculations (Figure S3, Supporting Information). They predict that the most energetically favored molybdenum carbides are MoC (–0.122 eV per atom) and Mo_2C (–0.140 eV per atom) followed by Mo_3C_2 and Mo_4C_3 with formation energies above 0.2 eV per atom. These calculations suggest that molybdenum carbide phases would be more likely than graphene and pure Mo forming. However, the calculations do not take into consideration any structural constraints which clearly do exist in this in situ study and moreover the influence from radiolysis and/or sputtering is not considered. This highlights the complexities of understanding dynamic processes of ordered double-transition metal MXenes under electron beam irradiation and shows further studies are needed for this exciting new family of 2D materials. This might include further studies with controlled temperatures, both in terms of elevated temperatures as well as reduced temperatures (viz. cooling) to help improve sample stability against electron irradiation induced damage as well as understand the various electron beam–specimen interactions in greater detail.

The stability of $Mo_2Ti_2C_3$ monolayer MXenes were examined under electron irradiation in a spherical aberration corrected TEM using 300 kV and 80 kV acceleration voltages. No significant changes are observed over the first 2 min of exposure to radiation. However, for extended irradiation periods beyond 2 min, structural changes are clearly observed. This included the formation of N-doped graphene membranes and ribbons, holes and Mo nanoribbons. The initial stability of $Mo_2Ti_2C_3$ and the subsequent rapid structural changes that occurred upon initial electron beam damage were demonstrated in the movies provided in the Supporting Information. During the in situ electron beam driven process, EELS results indicated preferential removal of Ti species. In some cases, C rearranged to form a graphene membrane or nanoribbon doped by N arising from residual TBA+ molecules from the delamination process. In other cases, Mo nanoribbons formed. Calculations (based on bulk structures) for formation energies show the situation is not straightforward since the suggested carbide formation might be preferential, however structural constraints are not considered in those calculations. The relatively easy surface diffusion of C and Mo species may have also been a consideration factor along with structural constrains (e.g., interfacing aspects). Moreover, at 300 kV, the in situ restructuring of the $Mo_2Ti_2C_3$ was more rapid than at 80 kV. This suggested that sputtering, and not radiolysis, was the primary driving mechanism for atom removal. However, a more specialized study is recommended to confirm this assessment. This study offered insight into the stability of $Mo_2Ti_2C_3$ monolayers against electron irradiation, which is important not only for understanding its characterization stability in TEM, but also for assessing its potential in the rapidly growing field of electron beam driven chemistry and engineering of nanomaterials.

Experimental Section

$Mo_2Ti_2C_3$ Synthesis: $Mo_2Ti_2C_3$ MXene was synthesized by the selective etching of aluminum layers from $Mo_2Ti_2AlC_3$[34] following a previously reported method.[42] $Mo_2Ti_2C_3$ powder was formed by gradually adding 2 g $Mo_2Ti_2AlC_3$ powder (particle size < 44 µm) to 20 mL 48–51% aqueous hydrofluoric acid (HF) solution over a 60 s period. The solution was stirred at 400 rpm with a magnetic Teflon coated bar at 55 °C for 96 h. The etchant solution was washed five times by adding deionized (DI) water, which entailed shaking for 60 s, centrifugation at 3500 rpm for 120 s for each cycle and decanting the supernatant until the pH was ≈6. After the last decanting, the remaining sediment was mixed with ≈10 mL of DI water and filtered using vacuum-assisted filtration on a porous membrane (Celgard, pore size 0.064 µm). The filtered product was the multilayered $Mo_2Ti_2C_3$ MXene powder used for the delamination process.

To delaminate $Mo_2Ti_2C_3$ powder to monolayer flakes, ≈1 g of the $Mo_2Ti_2C_3$ filtered powder and 10 mL TBAOH (40 wt% in water, Sigma-Aldrich) were stirred in a glass vial with a magnetic Teflon coated bar at 400 rpm for 4 h at room temperature. The basic mixture was washed twice with DI water via centrifugation at 3500 rpm for 120 s per cycle in a 50 mL centrifuge tube. 100 mL DI water was added to the sediment and the mixture was bath-sonicated (Branson 2510 Ultrasonic, 100 W) for 1 h, followed by centrifugation at 5000 rpm for 1 h in two 50 mL centrifuge tubes. The resulting supernatant containing mono- to few-layer $Mo_2Ti_2C_3$ MXene flakes was used for TEM imaging.

TEM Studies: Samples for TEM imaging were prepared by diluting ≈10 µL of the concentrated $Mo_2Ti_2C_3$ monolayer flake solution in 1 mL of distilled water. The diluted solution was bath-sonicated for 1 min at room temperature. ≈2 µL of the sonicated solution was drop coated on a copper TEM grid, coated with either a Lacey carbon or a quantifoil film. The grid offered support to the $Mo_2Ti_2C_3$ flakes during exposure to vacuum. The drop-coated grid was left to dry at room temperature for 2 h. The grid was then placed in high vacuum (≈10^{-6} mbar) at room temperature for about 3 h to remove any remaining water. The grid was transferred immediately from the high vacuum to the TEM column to minimize contamination. This process was repeated for each imaging sample, with a new sample used for each test. The images were obtained using a double Cs corrected FEI cubed Titan TEM working with a 300 kV acceleration voltage.

DFT Calculations: The first-principles DFT calculations were carried out by using the projector-augmented wave (PAW)[43] method and the Perdew–Burke–Ernzerhof (PBE) exchange correlation functional[44,45] as implemented in the Vienna ab initio Simulation Package (VASP).[46] The cutoff energy for the plane-wave basis set was 500 eV. The energy convergence criterion was chosen to be 10^{-6} eV. The Brillouin zones for Mo bulk and graphene were sampled using $15 \times 15 \times 15$ and $21 \times 21 \times 1$ *k*-point mesh. All the atoms were allowed to relax until the forces exerted on each atom were less than 0.01 eV $Å^{-1}$.

Supporting Information

Supporting Information is available from the Wiley Online Library or from the author.

Acknowledgements

This work was supported by the National Science Foundation China (NSFC, Project 51672181), the National Science Center, Poland for the financial support within the frame of the Opus program (Grant

agreement 2015/19/B/ST5/03399), and the Czech Republic from ERDF "Institute of Environmental Technology – Excellent Research" (No. CZ.02.1.01/0.0/0.0/16_019/0000853). M.H.R. and L.F. thank the Sino-German Research Institute for support (project: GZ 1400) and the start-up funding of the Suzhou Institute for Energy and Materials innovations (SIEMIS) and Suzhou University. B.A. thanks Bernard Haines for assisting him in MXene preparation. The authors are also grateful to Yury Gogotsi for support in obtaining the Mo2Ti2C3 MXene flakes and commentary.

Conflict of Interest

The authors declare no conflict of interest.

Keywords

electron driven chemistry, Mo nanoribbons, $Mo_2Ti_2C_3$, N-doped graphene, ordered double-transition metal MXenes

Received: December 5, 2019
Published online: January 14, 2020

[1] K. S. Novoselov, A. K. Geim, S. V. Morozov, D. Jiang, M. I. Katsnelson, I. V. Grigorieva, S. V. Dubonos, A. A. Firsov, *Science* **2004**, *306*, 666.
[2] Z.-Q. Wang, T.-Y. Lü, H.-Q. Wang, Y. P. Feng, J.-C. Zheng, *Front. Phys.* **2019**, *14*, 33403.
[3] A. Khandelwal, K. Mani, M. H. Karigerasi, I. Lahiri, *Mater. Sci. Eng., B* **2017**, *221*, 17.
[4] J. Pang, A. Bachmatiuk, Y. Yin, B. Trzebicka, L. Zhao, L. Fu, R. G. Mendes, T. Gemming, Z. Liu, M. H. Rummeli, *Adv. Energy Mater.* **2017**, 1702093.
[5] K. Zhang, Y. Feng, F. Wang, Z. Yang, J. Wang, *J. Mater. Chem. C* **2017**, *5*, 11992.
[6] S. Manzeli, D. Ovchinnikov, D. Pasquier, O. V. Yazyev, A. Kis, *Nat. Rev. Mater.* **2017**, *2*, 17033.
[7] T. Yang, T. T. Song, M. Callsen, J. Zhou, J. W. Chai, Y. P. Feng, S. J. Wang, M. Yang, *Adv. Mater. Interfaces* **2019**, *6*, 1801160.
[8] H. T. Tan, W. Sun, L. Wang, Q. Yan, *ChemNanoMat* **2016**, *2*, 562.
[9] G. Fiori, F. Bonaccorso, G. Iannaccone, T. Palacios, D. Neumaier, A. Seabaugh, S. K. Banerjee, L. Colombo, *Nat. Nanotechnol.* **2014**, *9*, 768.
[10] J. Pang, R. G. Mendes, A. Bachmatiuk, L. Zhao, H. Q. Ta, T. Gemming, H. Liu, Z. Liu, M. H. Rummeli, *Chem. Soc. Rev.* **2019**, *48*, 72.
[11] P. Zhang, F. Wang, M. Yu, X. Zhuang, X. Feng, *Chem. Soc. Rev.* **2018**, *47*, 7426.
[12] R. Kurapati, K. Kostarelos, M. Prato, A. Bianco, *Adv. Mater.* **2016**, *28*, 6052.
[13] M. Naguib, M. Kurtoglu, V. Presser, J. Lu, J. Niu, M. Heon, L. Hultman, Y. Gogotsi, M. W. Barsoum, *Adv. Mater.* **2011**, *23*, 4248.
[14] M. W. Barsoum, *MAX Phases: Properties of Machinable Ternary Carbides and Nitrides*, WILEY-VCH Verlag, Weinheim **2013**.
[15] M. Naguib, O. Mashtalir, J. Carle, V. Presser, J. Lu, L. Hultman, Y. Gogotsi, M. W. Barsoum, *ACS Nano* **2012**, *6*, 1322.
[16] M. Naguib, V. N. Mochalin, M. W. Barsoum, Y. Gogotsi, *Adv. Mater.* **2014**, *26*, 992.
[17] B. Anasori, M. R. Lukatskaya, Y. Gogotsi, *Nat. Rev. Mater.* **2017**, *2*, 16098.
[18] B. Anasori, Y. Xie, M. Beidaghi, J. Lu, B. C. Hosler, L. Hultman, P. R. C. Kent, Y. Gogotsi, M. W. Barsoum, *ACS Nano* **2015**, *9*, 9507.
[19] F. Shahzad, M. Alhabeb, C. B. Hatter, B. Anasori, S. M. Hong, C. M. Koo, Y. Gogotsi, *Science* **2016**, *353*, 1137.
[20] I. Persson, L. Å. Näslund, J. Halim, M. W. Barsoum, V. Darakchieva, J. Palisaitis, J. Rosen, P. O. Å. Persson, *2D Mater.* **2018**, *5*, 015002.
[21] X. Sang, X. Li, W. Zhao, J. Dong, C. M. Rouleau, D. B. Geohegan, F. Ding, K. Xiao, R. R. Unocic, *Nat. Commun.* **2018**, *9*, 2051.
[22] X. Sang, Y. Xie, D. E. Yilmaz, R. Lotfi, M. Alhabeb, A. Ostadhossein, B. Anasori, W. Sun, X. Li, K. Xiao, P. R. C. Kent, A. C. T. Van Duin, Y. Gogotsi, R. R. Unocic, *Nat. Commun.* **2018**, *9*, 1.
[23] J. Palisaitis, I. Persson, J. Halim, J. Rosen, P. O. Å. Persson, *Nanoscale* **2018**, *10*, 10850.
[24] M. H. Rummeli, H. Q. Ta, R. G. Mendes, I. G. Gonzalez-Martinez, L. Zhao, J. Gao, L. Fu, T. Gemming, A. Bachmatiuk, Z. Liu, *Adv. Mater.* **2019**, *31*, 1800715.
[25] M. H. Rummeli, Y. Pan, L. Zhao, J. Gao, H. Q. Ta, I. G. Martinez, R. G. Mendes, T. Gemming, L. Fu, A. Bachmatiuk, Z. Liu, *Materials* **2018**, *11*, 896.
[26] C. Elbadawi, T. T. Tran, M. Kolíbal, T. Šikola, J. Scott, Q. Cai, L. H. Li, T. Taniguchi, K. Watanabe, M. Toth, I. Aharonovich, C. Lobo, *Nanoscale* **2016**, *8*, 16182.
[27] J. Kotakoski, C. H. Jin, O. Lehtinen, K. Suenaga, A. V. Krasheninnikov, *Phys. Rev. B* **2010**, *82*, 113404.
[28] R. G. Mendes, J. Pang, A. Bachmatiuk, H. Q. Ta, L. Zhao, T. Gemming, L. Fu, Z. Liu, M. H. Rümmeli, *ACS Nano* **2019**, *13*, 978.
[29] M. H. Rümmeli, H. Q. Ta, R. G. Mendes, I. G. Gonzalez-Martinez, L. Zhao, J. Gao, L. Fu, T. Gemming, A. Bachmatiuk, Z. Liu, *Adv. Mater.* **2018**, *30*, 1800715.
[30] D. Zhang, Y. Zhu, L. Liu, X. Ying, C. Hsiung, R. Sougrat, K. Li, Y. Han, *Science* **2018**, *359*, 675.
[31] M. Seredych, C. E. Shuck, D. Pinto, M. Alhabeb, E. Precetti, G. Deysher, B. Anasori, N. Kurra, Y. Gogotsi, *Chem. Mater.* **2019**, *31*, 3324.
[32] J. L. Hart, K. Hantanasirisakul, A. C. Lang, B. Anasori, D. Pinto, Y. Pivak, J. T. van Omme, S. J. May, Y. Gogotsi, M. L. Taheri, *Nat. Commun.* **2019**, *10*, 522.
[33] X. Sang, Y. Xie, M. W. Lin, M. Alhabeb, K. L. Van Aken, Y. Gogotsi, P. R. C. Kent, K. Xiao, R. R. Unocic, *ACS Nano* **2016**, *10*, 9193.
[34] B. Anasori, M. Dahlqvist, J. Halim, E. J. Moon, J. Lu, B. C. Hosler, E. N. Caspi, S. J. May, L. Hultman, P. Eklund, J. Rosén, M. W. Barsoum, *J. Appl. Phys.* **2015**, *118*, 0.
[35] F. Börrnert, S. M. Avdoshenko, A. Bachmatiuk, I. Ibrahim, B. Büchner, G. Cuniberti, M. H. Rümmeli, *Adv. Mater.* **2012**, *24*, 5630.
[36] R. G. Mendes, A. Bachmatiuk, A. A. El-Gendy, S. Melkhanova, R. Klingeler, B. Büchner, M. H. Rümmeli, *J. Phys. Chem. C* **2012**, *116*, 23749.
[37] H. P. Komsa, S. Kurasch, O. Lehtinen, U. Kaiser, A. V. Krasheninnikov, *Phys. Rev. B: Condens. Matter Mater. Phys.* **2013**, *88*, 035301.
[38] J. Lin, Y. Zhang, W. Zhou, S. T. Pantelides, *ACS Nano* **2016**, *10*, 2782.
[39] X. Liu, T. Xu, X. Wu, Z. Zhang, J. Yu, H. Qiu, J.-H. Hong, C.-H. Jin, J.-X. Li, X.-R. Wang, L.-T. Sun, W. Guo, *Nat. Commun.* **2013**, *4*, 1776.
[40] J. Jia, W. Zhou, G. Li, L. Yang, Z. Wei, L. Cao, Y. Wu, K. Zhou, S. Chen, *ACS Appl. Mater. Interfaces* **2017**, *9*, 8041.
[41] T. Wang, X. Tian, Y. Yang, Y. W. Li, J. Wang, M. Beller, H. Jiao, *Phys. Chem. Chem. Phys.* **2016**, *18*, 6005.
[42] B. Anasori, C. Shi, E. J. Moon, Y. Xie, C. A. Voigt, P. R. C. Kent, S. J. May, S. J. L. Billinge, M. W. Barsoum, Y. Gogotsi, *Nanoscale Horiz.* **2016**, *1*, 227.
[43] P. E. Blöchl, *Phys. Rev. B* **1994**, *50*, 17953.
[44] J. P. Perdew, K. Burke, M. Ernzerhof, *Phys. Rev. Lett.* **1996**, *77*, 3865.
[45] G. Kresse, D. Joubert, *Phys. Rev. B* **1999**, *59*, 1758.
[46] G. Kresse, J. Furthmüller, *Phys. Rev. B: Condens. Matter Mater. Phys.* **1996**, *54*, 11169.